

Enhanced State Estimation for Wheeled Vehicles

Paul F. Roysdon

Jay A. Farrell

David Kelley

P. F. Roysdon earned B.S. degrees in aeronautical and mechanical engineering from the University of California, Davis, and M.S. degrees in aeronautical and mechanical engineering from the Von Karman Institute for Fluid Dynamics, Belgium, and the University of California, Davis, respectively. He is currently completing M.S. and Ph.D. degrees in electrical engineering from the University of California, Riverside. He worked for Composite Engineering Inc. (now Kratos Defense & Security Systems) from 2005-2015 as a Research Engineer in the Advanced Programs division, developing high-performance subsonic and supersonic UAV's. While at CEi, he contributed to the various stages of development from conceptual design through production, supporting military operations for the US Air Force, Army and Navy. Contributions included: aircraft layout and design, guidance and control algorithms, and co-authored CEi's GPS-INS navigation system, which was fielded on two of their UAV production lines. He is a Senior Member of the AIAA, and serves on the AIAA Aircraft Design Technical Committee (2006-Present). He is also a Member of the IEEE and ION, and the author of several technical articles. <proysdon@ee.ucr.edu>

J. A. Farrell earned B.S. degrees in physics and electrical engineering from Iowa State University, and M.S. and Ph.D. degrees in electrical engineering from the University of Notre Dame. After working at Charles Stark Draper Lab (1989-1994), he joined the University of California, Riverside. He is a Professor and two time Chair of the Department of Electrical and Computer Engineering. He has served the IEEE Control Systems Society on their Board of Governors for two terms ('03-'06, '12-'14), as Vice President Finance and Vice President of Technical Activities, as General Chair for IEEE CDC 2012, and as President in 2014. He was named a GNSS Leader to Watch for 2009-2010 by GPS World Magazine in May 2009. He is a Fellow of the IEEE, a Fellow of AAAS, a Distinguished Member of IEEE CSS, and author of over 250 technical articles and three books. <farrell@ee.ucr.edu>

D. Kelley is Director of ITS Programs for SubCarrier Systems in Glendora, California. He received his BS in electrical engineering from the University of Missouri-Rolla (now Missouri S&T) in 1983. His first exposure to GNSS was in 1984 developing GPS correlators for military avionics applications while employed by Texas Instruments. In 1988 he founded Terrapin, a firm using commercial radio beacons for an alternative means of navigation. He has been developing various RTK navigation methods for use in the ground automotive market segment for the past 25 years. In the area of intelligent transportation systems

(ITS) Mr Kelley is active in developing many of the key standards used between vehicles and the roadside for advanced safety systems which employ GNSS. He, and SCSC, are active members of RTCM, ION, IEEE, and SAE. He is an expert to the US delegation of ISO TC204 for telematics matters. He holds multiple patents for differential navigation methods using terrestrial signals of opportunity. His current research interests involve low cost L1 only RTK development. <DavidKelley@itsware.net>

Abstract—Accurate state estimation for wheeled vehicles is valuable for a wide variety of applications from vehicle stability-control to life-safety critical systems. Commonly applied GNSS-encoder state estimation approaches like the Extended Kalman Filter can be challenged when addressing the issue of significantly corrupted data, due to limited measurement redundancy. One approach to increasing measurement redundancy is to include additional sensors like Inertial Measurement Units (IMU's), cameras and LiDARs. This paper presents an alternative approach, leveraging a minimal set of sensors which are already installed on most modern mass-production vehicles, and requiring only a software update. We propose a sliding window, nonlinear, *Maximum-a-Posteriori* estimator to solve the GNSS-encoder navigation problem. The sliding window implementation provides sufficient redundancy to enable detection and compensation of various measurement anomalies. While this paper focuses on automotive applications, this method applies to any wheeled vehicle (e.g. rovers, trains, commercial equipment).

I. INTRODUCTION

Factors limiting state estimation accuracy and reliability for wheeled vehicles equipped with encoders include road surface unevenness, unmodeled roll dynamics, and wheel slip [1]–[4]. The accumulation of errors in dead-reckoning approaches is especially critical in urban environments where GNSS aiding signals are not always available and may be significantly corrupted. This article presents a novel real-time estimation approach solving the full nonlinear *Maximum A Posteriori* (MAP) problem incorporating information from encoders and GNSS over a time window of varying length [5], [6]. The approach will be demonstrated through the simulation of rotary wheel encoders and a GNSS receiver.

Accurate state estimation provides valuable information for a wide variety of applications such as the driver assistance [7], stability control systems [8] and other safety systems found in many modern vehicles. Current applications [9] either restrict their systems to changes in wheel encoders uncoupled from GNSS, or apply more expensive sensing technologies, such as computer vision or LiDAR [10]–[12], to solve the problem of accurate state estimation. In contrast this work seeks to maximize the accuracy and reliability achievable from a minimal set of sensors already installed on

most vehicles today. This is achieved through more extensive real-time optimization and error detection; instead of more expensive sensors. This approach offers immediate application with minimal modification to existing vehicle systems. In fact, many premium mass production vehicle models (e.g. BMW, Mercedes-Benz, Lexus and Acura) come already equipped with processors capable of high performance computing, and would only require a software upgrade to enable the use of this estimator.

The following sections discuss the theoretical basis for GNSS-encoder navigation and compare results of the Extended Kalman Filter (EKF) and MAP estimator (optimal for the nonlinear model). The paper specifically addresses the real-world conditions for unequal tire pressure, wheel slip, as well as the urban canyon and viaducts and their influence on GNSS availability and reliability. The results demonstrate improved performance of the MAP estimator over the commonly applied EKF in GNSS-encoder based navigation. This improved performance is attributed to the extended window of available GNSS epochs, which enhances the ability to detect and accommodate errors, and the ability of the nonlinear MAP approach to correct linearization errors due to poor initialization and the effects of past missed detections. This improvement eliminates the need for many of the previously proposed heuristics for estimating wheel radii and wheel base [13]. Additionally, the approach may alleviate the need for vehicle-level calibration [14].

II. SYSTEM OVERVIEW

This section provides the theoretical description of the GNSS-encoder navigation problem, see Ch. 9 in [15].

A. Encoder Navigation Theory

Let $\mathbf{x} \in \mathbb{R}^n$, where $n = 7$, denote the vehicle state vector. The navigation system maintains the estimated state vector

$$\hat{\mathbf{x}} = [\hat{g}\hat{\mathbf{p}}_I^\top \quad \hat{\mathbf{a}}_I^\top \quad \hat{\mathbf{b}}_w^\top]^\top \quad (1)$$

where $\hat{g}\hat{\mathbf{p}}_I \in \mathbb{R}^3$ is the vehicle position (n , e , d) in geographic frame, $\hat{\mathbf{a}}_I \in \mathbb{R}^2$ is the Euler attitude (θ , ψ) for simplicity we will consider $\phi = 0$, and $\hat{\mathbf{b}}_w \in \mathbb{R}^2$ are the rear-wheel radii (R_l , R_r) left and right respectively.

The kinematic equations for the vehicle state are described by

$$\dot{\mathbf{x}}(t) = \mathbf{f}(\mathbf{x}(t), \mathbf{u}(t)), \quad (2)$$

where $\mathbf{f} : \mathbb{R}^n \times \mathbb{R}^m \mapsto \mathbb{R}^n$ and $\mathbf{u} \in \mathbb{R}^m$ is the vector of $m = 2$ encoder measurements. The function \mathbf{f} is accurately known (see eqns. (9.44) and (9.45) in [15]). Nature integrates eqn. (2) to produce $\mathbf{x}(t)$.

Assume there is a prior for the first state: $\mathbf{x}(t_0) \sim \mathcal{N}(\mathbf{x}_0, \mathbf{P}_0)$. The corresponding residual function is

$$\epsilon_0(\mathbf{x}(t_0)) = \mathbf{x}(t_0) - \mathbf{x}_0. \quad (3)$$

Given this distribution and measurements $\tilde{\mathbf{u}}$ of \mathbf{u} , a navigation system propagates an estimate of the vehicle state between aiding measurement times as a solution of

$$\dot{\hat{\mathbf{x}}}(t) = \mathbf{f}(\hat{\mathbf{x}}(t), \tilde{\mathbf{u}}(t)), \quad (4)$$

where $\hat{\mathbf{x}}(t)$ denotes the real-time estimate of $\mathbf{x}(t)$.

Let $t_k = kT$ denote the time instants at which GNSS measurements are valid. Let τ_i denote the time instants at which encoder measurements are valid. It is typically the case that $T \gg [\tau_i - \tau_{i-1}]$. Therefore, there are numerous encoder measurements available between GNSS epochs. For a variable $a(t)$, to simplify notion, define $a_i \triangleq a(\tau_i)$ and $a_k \triangleq a(t_k)$. Define $\mathbf{U}_k \triangleq \{\tilde{\mathbf{u}}_i | \tau_i \in [t_{k-1}, t_k]\}$

The solution of (4) over the interval $t \in [\tau_{i-1}, \tau_i]$ from the initial condition \mathbf{x}_{i-1} is represented as the operator:

$$\phi(\mathbf{x}_{i-1}, \mathbf{u}_{i-1}) = \mathbf{x}_{i-1} + \int_{t_{i-1}}^{t_i} \mathbf{f}(\mathbf{x}(\tau), \mathbf{u}(\tau)) d\tau. \quad (5)$$

This integral operator can be iterated for all encoder measurements in \mathbf{U}_k to propagate the state from t_{k-1} to t_k . The iterated integral operation is denoted as

$$\hat{\mathbf{x}}_k = \mathbf{F}(\hat{\mathbf{x}}_{k-1}, \mathbf{U}_k). \quad (6)$$

B. Encoder Navigation Details

The linear velocity (positive in the forward direction) \hat{u} , and rotational velocity (positive clockwise) \hat{w} , are computed as

$$\hat{u} = \frac{\pi}{\mathcal{N}} \left(\hat{R}_l \Delta e_l + \hat{R}_r \Delta e_r \right) \quad (7)$$

$$\hat{w} = \frac{2\pi}{\mathcal{L}\mathcal{N}} \left(\hat{R}_l \Delta e_l - \hat{R}_r \Delta e_r \right) \quad (8)$$

where \mathcal{N} is the fixed number of encoder increments per revolution, \mathcal{L} is the width of the wheel base, \hat{R}_l and \hat{R}_r are the estimated left and right rear wheel radii, e_l and e_r are the left and right encoder increments at t_i , Δe_l and Δe_r are the total left and right encoder increments over the time interval $t \in [\tau_{i-1}, \tau_i]$, defined as

$$\Delta e_l(\tau_i) = e_l(\tau_i) - e_l(\tau_{i-1}) \quad (9)$$

$$\Delta e_r(\tau_i) = e_r(\tau_i) - e_r(\tau_{i-1}) \quad (10)$$

C. Error Model

Due to initial condition errors, system calibration errors, and measurement noise, an estimation state error $\delta\mathbf{x}(t) = \mathbf{x}(t) - \hat{\mathbf{x}}(t)$ develops over time. The error state vector is

$$\delta\mathbf{x} = [\delta\dot{n}, \delta\dot{e}, \delta\dot{d}, \delta\dot{\theta}, \delta\dot{\psi}, \delta\dot{R}_l, \delta\dot{R}_r]^\top.$$

The position error propagation model is

$$\begin{aligned} \delta\dot{n} = & \frac{1}{2} \cos \hat{\psi} \cos \hat{\theta} \left(\frac{\hat{u}_l}{\hat{R}_l} \delta R_l + \frac{\hat{u}_r}{\hat{R}_r} \delta R_r \right) - \hat{u} \cos \hat{\psi} \cos \hat{\theta} \delta \theta \\ & - \hat{u} \sin \hat{\psi} \cos \hat{\theta} \delta \psi + \omega_n \end{aligned} \quad (11)$$

$$\begin{aligned} \delta\dot{e} = & \frac{1}{2} \sin \hat{\psi} \cos \hat{\theta} \left(\frac{\hat{u}_l}{\hat{R}_l} \delta R_l + \frac{\hat{u}_r}{\hat{R}_r} \delta R_r \right) - \hat{u} \sin \hat{\psi} \sin \hat{\theta} \delta \theta \\ & + \hat{u} \cos \hat{\psi} \cos \hat{\theta} \delta \psi + \omega_e \end{aligned} \quad (12)$$

$$\delta\dot{d} = \frac{1}{2} \sin \hat{\theta} \left(\frac{\hat{u}_l}{\hat{R}_l} \delta R_l + \frac{\hat{u}_r}{\hat{R}_r} \delta R_r \right) - \hat{u} \cos \hat{\theta} \delta \theta + \omega_d. \quad (13)$$

The attitude error propagation model is

$$\delta\dot{\theta} = \omega_\theta \quad (14)$$

$$\begin{aligned} \delta\dot{\psi} = & \frac{\cos \hat{\phi}}{\mathcal{L} \cos \hat{\theta}} \left(\left(\frac{\hat{u}_l}{\hat{R}_l} \delta R_l - \frac{\hat{u}_r}{\hat{R}_r} \delta R_r \right) - \hat{w} \sin \hat{\phi} \delta \phi \right. \\ & \left. + \hat{w} \cos \hat{\phi} \tan \hat{\theta} \delta \theta \right) + \omega_\psi. \end{aligned} \quad (15)$$

The wheel radii error propagation model is selected to be

$$\delta\dot{R}_l = -\lambda_R \delta R_l + \omega_l \quad (16)$$

$$\delta\dot{R}_r = -\lambda_R \delta R_r + \omega_r. \quad (17)$$

The symbols \hat{u}_l and \hat{u}_r represent the estimated velocities at the wheel center of the rear wheels (left and right). The correlation time of the wheel radii is $1/\lambda_R$. The symbol $\omega = [\omega_n, \omega_e, \omega_d, \omega_\theta, \omega_\psi, \omega_l, \omega_r]^\top$ represents the driving noise vector processes. The diagonal of the power spectral density (PSD) matrix is $[\sigma_n^2, \sigma_e^2, \sigma_d^2, \sigma_\theta^2, \sigma_\psi^2, \sigma_l^2, \sigma_r^2]$. The estimated pitch and heading, are $\hat{\theta}$, $\hat{\psi}$. The estimated roll is defined as $\hat{\phi} = 0$.

The linearized version of the operator in eqn. (6) predicts the propagation of the error state over the discrete-time interval $t \in [t_{k-1}, t_k]$ according to the standard model

$$\delta\hat{\mathbf{x}}_k = \Phi_{k-1} \delta\hat{\mathbf{x}}_{k-1} + \omega_{k-1} \quad (18)$$

where $\mathbf{Qd}_k = \text{cov}(\omega_k)$ is the covariance of the discrete-time process noise $\omega_k \sim N(0, \mathbf{Qd}_k)$, and Φ_{k-1} is the linearization of $\phi(\mathbf{x}_{i-1}, \mathbf{u}_{i-1})$ accumulated over the time interval $t \in [t_{k-1}, t_k]$. Computation of both \mathbf{Qd}_k and Φ_{k-1} is based on the linearized continuous-time error state model

$$\delta\dot{\mathbf{x}}(t) = \mathbf{A}\delta\mathbf{x} + \mathbf{B}\omega. \quad (19)$$

The matrices \mathbf{A} and \mathbf{B} can be derived from eqns. (11- 17). The implementation process is discussed in Sections 4.7.1 and 7.2.5.2 of [15].

The encoder kinematic constraint ϵ_e^k between state \mathbf{x}_{k-1} and \mathbf{x}_k is

$$\epsilon_e^k(\mathbf{x}_{k-1}, \mathbf{x}_k) = \mathbf{x}_k - \mathbf{F}(\mathbf{x}_{k-1}, \mathbf{U}_k). \quad (20)$$

The uncertainty of ϵ_e^k is defined by the covariance of ω_k .

D. GNSS Model

The GNSS pseudorange measurement vector \mathbf{y} at t_k is modeled as

$$\mathbf{y}_k = \mathbf{h}(\mathbf{x}_k) + \boldsymbol{\eta}_{\rho k}. \quad (21)$$

Using state estimate, the GNSS pseudorange measurements at t_k is predicted to be

$$\hat{\mathbf{y}}_k = \mathbf{h}(\hat{\mathbf{x}}_k). \quad (22)$$

The GNSS measurement residual vector is computed as

$$\delta\mathbf{y}_k = \mathbf{y}_k - \hat{\mathbf{y}}_k, \quad (23)$$

and modeled as

$$\delta\mathbf{y}_k = \mathbf{H}_k \delta\mathbf{x}_k + \boldsymbol{\eta}_k \quad (24)$$

where \mathbf{H}_k is the Jacobian of $\mathbf{h}(\hat{\mathbf{x}}_k)$ computed at $\hat{\mathbf{x}}_k$.

The GNSS pseudorange measurement constraint ϵ_y^k is

$$\epsilon_y^k(\mathbf{x}_k) = \mathbf{y}_k - \mathbf{h}(\mathbf{x}_k). \quad (25)$$

The uncertainty of $\epsilon_y^k(\mathbf{x}_k)$ is defined by the covariance of $\boldsymbol{\eta}_k$ which is assumed to be Gaussian with the variance denoted by $\sigma_\rho^2 \mathbf{I}$.

III. MAP ESTIMATION

A sliding-window real-time smoothing approach is used to integrate the GPS and encoder data. The Contemplative Real-Time (CRT) estimator [16] has both real-time and contemplative aspects. The real-time state estimate is required for control and planning purposes, without latency. The contemplative aspects are intended to enhance accuracy and reliability. The sliding window smoother is inspired by recent research in the field of robotics literature, see e.g. [17]–[19].

The primary advantages of the CRT approach are:

- 1) It computes the optimal nonlinear MAP solution for a temporal window of sensor data.
- 2) It has the ability to correct the linearization point of the trajectory within the CRT window.
- 3) The set of residuals accumulated from the prior in eqn. (3), encoder in eqn. (20), and GNSS constraints in eqn. (25) provide enhanced opportunities to detect and remove the effects of anomalous sensor data.

In comparison, the EKF only performs the linearization once and the linearization point of the past trajectory cannot be changed when new measurements are obtained or faults are detected in the current measurement. We present five examples in Section V.

A. Theoretical Solution

Let \mathbf{X}_k denote the vehicle trajectory over a time window

$$\mathbf{X} = [\mathbf{x}(t_{k-L})^\top \cdots \mathbf{x}(t_k)^\top]^\top \quad (26)$$

where L is the window size. Without loss of generality (WOLG), in the following, we will let $k = L$.

Estimation of the vehicle trajectory \mathbf{X} can be formulated as a *Maximum A Posteriori* (MAP) problem (see Ch. 11.5 of [20]):

$$\hat{\mathbf{X}} = \underset{\mathbf{X}}{\operatorname{argmax}} \{p(\mathbf{X}, \mathbf{U}, \mathbf{Y})\} \quad (27)$$

where $\mathbf{U} = \{\mathbf{U}_j | j \in [0, k]\}$ is the high rate encoder data within the time window, and $\mathbf{Y} = \{\mathbf{y}_j | j \in [0, k]\}$ is the GNSS pseudorange measurements. The joint probability for the GNSS-encoder problem, $p(\mathbf{X}, \mathbf{U}, \mathbf{Y})$, can be decomposed as

$$\begin{aligned} p(\mathbf{X}, \mathbf{U}, \mathbf{Y}) = & p(\mathbf{x}_0) \prod_{i=0}^{k-1} p(\mathbf{x}_{i+1} | \mathbf{x}_i, \mathbf{U}_{i+1}) \prod_{j=1}^k p(\mathbf{y}_j | \mathbf{x}_j), \end{aligned} \quad (28)$$

where $p(\mathbf{x}_0)$ is the distribution of the initial condition defined in eqn. (3), $p(\mathbf{x}_{i+1} | \mathbf{x}_i, \mathbf{U}_{i+1})$ is the distribution of the kinematic constraint in eqn. (20), and $p(\mathbf{y}_j | \mathbf{x}_j)$ is the distribution of the pseudorange measurement constraint in eqn. (25).

Assuming that the noise terms have Gaussian distributions, using log-likelihood, the MAP estimation problem can be converted to an equivalent nonlinear least squares problem:

$$\hat{\mathbf{X}} = \underset{\mathbf{X}}{\operatorname{argmin}} \left\{ \sum_{s \in \mathbb{S}} \|\epsilon_s(\mathbf{X})\|_{\mathbf{W}_s}^2 \right\} \quad (29)$$

where $\epsilon_s(\mathbf{X})$ is the vector residual function defined for all the information available (denoted by the set \mathbb{S}). The set \mathbb{S} contains the constraints of eqns. (3), (20), and (25). The matrix \mathbf{W}_s is positive definite with block diagonal entries defined by \mathbf{P}_0 , $\mathbf{Q}d_k$, and $\sigma_\rho^2 \mathbf{I}$. The symbol $\|\cdot\|_{\mathbf{W}_s}^2$ denotes the squared Mahalanobis norm: $\|\mathbf{x}\|_{\mathbf{Z}}^2 = \mathbf{x}^\top \mathbf{Z}^{-1} \mathbf{x}$ for positive definite \mathbf{Z} .

B. Nonlinear Least Squares Problem

To solve the nonlinear least squares optimization problem, at each iteration, we solve the linearized normal equation

$$\mathbf{J}^\top \mathbf{J} \delta \mathbf{X} = \mathbf{J}^\top \mathbf{b} \quad (30)$$

which can be compactly expressed as

$$\Lambda \delta \mathbf{X} = \zeta \quad (31)$$

where $\Lambda = \mathbf{J}^\top \mathbf{J}$ is the information matrix, $\zeta = \mathbf{J}^\top \mathbf{b}$ is the information vector, \mathbf{J} is the normalized Jacobian matrix and \mathbf{b} is the normalized residual vector. As shown in [5], \mathbf{J} is a sparse, block diagonal, matrix. Eqn. (30) can be solved efficiently by many methods, e.g. Cholesky, QR, or SVD (see [5], [18], [19]).

C. Outlier Detection and Mitigation

The simulation experiments will consider two types of errors: wheel slip and GNSS outliers.

Wheel Encoders. We define a function $\nu(\Delta e_l, \Delta e_r)$ of the change in wheel encoder counts, such that when the vehicle maneuvers, $\nu(\Delta e_l, \Delta e_r)$ is approximately zero. An example function could be

$$\nu(\Delta e_l, \Delta e_r) = \left| \frac{\Delta e_l}{\Delta e_r} \right| - 1$$

for $\Delta e_r \neq 0$. A constant detection threshold μ_e is selected such that

$$-\mu_e \leq \nu(\Delta e_l, \Delta e_r) \leq \mu_e$$

even when the vehicle turns in either direction at its minimum turning radius. A wheel encoder outlier is detected when $|\nu(\Delta e_l, \Delta e_r)| > \mu_e$. When an encoder outlier is detected, mitigation is performed by increasing the values for the elements of \mathbf{Q} corresponding to the encoder measurements (i.e. $\mathbf{Q}_i(1, 1) = 1e^{12}$, and $\mathbf{Q}_i(2, 2) = 1e^{12}$), thus effectively eliminating their influence in \mathbf{J} of eqn. (30).

GNSS. The outlier detection algorithm for GNSS measurements, evaluates the elements of the residuals vector \mathbf{b} of eqn. (30) against a threshold μ_g . For any detected $\mathbf{b}_j > \mu_g$ the corresponding GNSS pseudorange measurements are removed from the rows of ζ and Λ , and the NLLS optimization is repeated.

IV. OBSERVABILITY ANALYSIS

Consider the observability 3D GNSS-Encoder navigation problem, where the residual measurement vector is

$$\delta \mathbf{y} = \mathbf{H} \delta \mathbf{x} + \boldsymbol{\eta}. \quad (32)$$

Assuming WOLG that we can measure position, then

$$\mathbf{H} = \begin{bmatrix} 1 & 0 & 0 & 0 & 0 & 0 & 0 \\ 0 & 1 & 0 & 0 & 0 & 0 & 0 \\ 0 & 0 & 1 & 0 & 0 & 0 & 0 \end{bmatrix}. \quad (33)$$

With \mathbf{A} from eqn. (19) evaluated around $\phi = 0$ and $\theta = 0$, the linear observability matrix

$$\mathcal{O} = \begin{bmatrix} \mathbf{H} \\ \mathbf{H}\mathbf{A} \\ \mathbf{H}\mathbf{A}^2 \end{bmatrix} \quad (34)$$

yields eqn. (35), which allows analysis of several specific cases unique to this problem.

For $u = \omega = 0$, it is the case that $u_l = u_r = 0$. Therefore, columns (4-7) in eqn. (35) are zero. The matrix \mathcal{O} has rank 3. Only the position states are observable. The unobservable subspace includes the attitude errors (θ, ψ) as well as wheel radii errors (R_l, R_r).

When $u \neq 0$, an orthogonal basis for the observable space (see Sect. 3.6.3 in [15]) are the columns of the matrix

$$\mathbf{W}_o = \begin{bmatrix} 1 & 0 & 0 & 0 & 0 & 0 \\ 0 & 1 & 0 & 0 & 0 & 0 \\ 0 & 0 & 1 & 0 & 0 & 0 \\ 0 & 0 & 0 & u & 0 & 0 \\ 0 & 0 & 0 & 0 & u & 0 \\ 0 & 0 & 0 & 0 & 0 & \hat{u}_l \hat{R}_r \\ 0 & 0 & 0 & 0 & 0 & \hat{u}_r \hat{R}_l \end{bmatrix}. \quad (36)$$

A basis for the unobservable space is the vector

$$\mathbf{W}_u = [0, 0, 0, 0, 0, -\hat{u}_l \hat{R}_r, \hat{u}_r \hat{R}_l]^\top \quad (37)$$

Therefore, we see that the grade and yaw are observable. For any fixed values of u_l and u_r , there is a linear combination of the wheel radii that is observable and an orthogonal complement that is not observable. As the vehicle maneuvers, the specific values of u_l and u_r vary with time, changing the observable and unobservable subspaces, resulting in the ability to independently estimate the wheel radii.

V. SIMULATION RESULTS

For simulation analysis of the performance of the MAP estimator, we create a ground truth vehicle trajectory $\mathbf{x}(t)$ and noise corrupted encoder measurements at 100Hz. Similarly, from the GNSS measurement equations, we can generate noise corrupted raw GNSS observables and ephemerids at 1 Hz as obtained from RINEX observation (.obs) and navigation (.nav) files, for any given day. Thus for any desired 3D trajectory, we have a complete set of synthetic measurements for evaluation.

In the examples, the sliding window contains $L = 20$ epochs, starting with a single measurement at t_1 seconds,

$$\mathcal{O} = \begin{bmatrix} 1 & 0 & 0 & 0 & 0 & 0 & 0 & 0 \\ 0 & 1 & 0 & 0 & 0 & 0 & 0 & 0 \\ 0 & 0 & 1 & 0 & 0 & 0 & 0 & 0 \\ 0 & 0 & 0 & 0 & -\hat{u} \sin \hat{\psi} & \frac{\hat{u}_l}{2\hat{R}_l} \cos \hat{\psi} & \frac{\hat{u}_r}{2\hat{R}_r} \cos \hat{\psi} & 0 \\ 0 & 0 & 0 & 0 & \hat{u} \cos \hat{\psi} & \frac{\hat{u}_l}{2\hat{R}_l} \sin \hat{\psi} & \frac{\hat{u}_r}{2\hat{R}_r} \sin \hat{\psi} & 0 \\ 0 & 0 & 0 & -\hat{u} & 0 & 0 & 0 & 0 \\ 0 & 0 & 0 & 0 & 0 & -\frac{\hat{u}_l}{\hat{R}_l} \left(\frac{\hat{u} \sin \hat{\psi}}{L} + \frac{\cos \hat{\psi} \lambda_R}{2} \right) & -\frac{\hat{u}_r}{\hat{R}_r} \left(\frac{\hat{u} \sin \hat{\psi}}{L} + \frac{\cos \hat{\psi} \lambda_R}{2} \right) & 0 \\ 0 & 0 & 0 & 0 & 0 & \frac{\hat{u}_l}{\hat{R}_l} \left(\frac{\hat{u} \cos \hat{\psi}}{L} - \frac{\sin \hat{\psi} \lambda_R}{2} \right) & \frac{\hat{u}_r}{\hat{R}_r} \left(\frac{\hat{u} \cos \hat{\psi}}{L} - \frac{\sin \hat{\psi} \lambda_R}{2} \right) & 0 \\ 0 & 0 & 0 & 0 & 0 & 0 & 0 & 0 \end{bmatrix} \quad (35)$$

and building the window over the interval $t_{1,\dots,20}$, before sliding the window at $t_{2,\dots,21}$. The initial covariance matrix is $\mathbf{P}(0) = \text{diag}([4^2, 4^2, 1^2, 0.1^2, 0.5^2, 0.008^2, 0.008^2])$, and GNSS measurement error covariance is $\mathbf{R}(0) = 0.25^2 \mathbf{I}_{12 \times 12}$. If not otherwise stated, the initial state is $\mathbf{x} = [0, 0, 0, 0^\circ, 0^\circ, 0.3048, 0.3048]$, $\mathcal{L} = 1.524\text{m}$, and $\mathcal{N} = 25$. The number of iterations required for convergence of the MAP estimator is plotted for each example, typically 2 iterations are necessary, with a maximum of 7 iterations observed during all the examples.

Each example uses the same simulation trajectory (with perturbed conditions appropriate to each example). The vehicle accelerates from rest at t_0 to 20 m/s at t_{10} , then at t_{30} ascends a hill with 10 degrees grade (i.e. pitch angle) to 100 meters elevation. From t_{70} to t_{290} , three straight legs are performed with 180 degree banked turns in between, with a road bank angle of 10 degrees in the turns and 0 otherwise. At t_{300} the vehicle then descends a hill with -10 degrees grade, returning to 0 meters elevation, followed by a level deceleration to rest at t_{370} . Figure 1 displays the nominal 3D trajectory results for the three state estimators against truth.

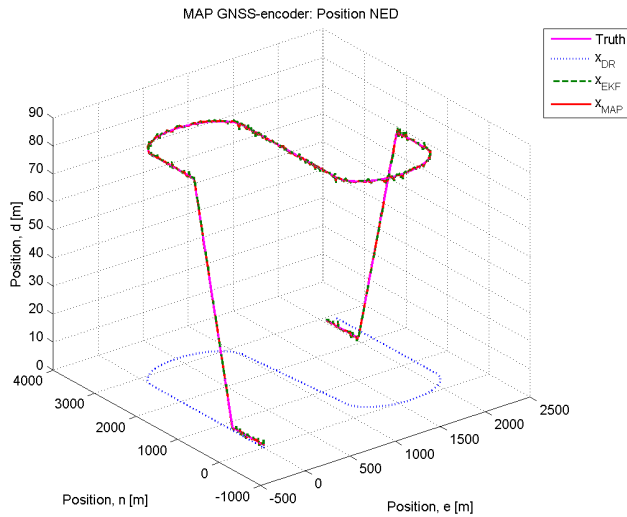


Fig. 1. Simulated 3D trajectory. EKF and MAP closely overlay the ground truth, while DR accumulates 3D positional error due to the lack of elevation and grade estimation.

we plot components of the state estimation error relative to the ground truth trajectory e.g. $\Delta = \|\mathbf{S}\delta\mathbf{x}(t)\|$ versus time, where \mathbf{S} is a matrix that selects specific elements of $\delta\mathbf{x}$.

A. Initialization Error

This example considers a large yaw angle initialization error, where $\mathbf{x}(0) = [10, 10, 2, 10^\circ, 180^\circ, 0.35, 0.35]$ and $\hat{\mathbf{x}}(0) = 0$. The north and east position errors, yaw attitude error, and number of iterations are shown in Figure 2. Notice the dead-reckoning (DR) algorithm diverges and never recovers. The EKF attempts to correct the large error in a single iteration; however, the linearization point is incorrect and the EKF performance suffers. The MAP corrects the error at the first GNSS epoch after the velocity becomes non-zero.

At time steps $t = 0$ and $t = 1$, both the EKF and the MAP have equivalent information (i.e. one epoch of aiding measurements). Both have the same prior $\hat{\mathbf{x}}(0)$. The only difference between them is the nonlinear optimization of the MAP (i.e. the iterated Kalman Filter), which enables the MAP to correct the linearization point.

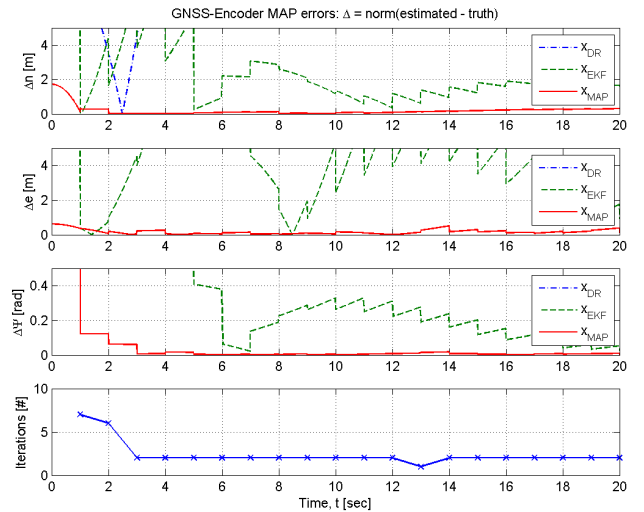


Fig. 2. Initial yaw error of 180° results in a constant DR error, and the EKF is unreliable for 120 sec., while MAP removes the error within 1 GNSS epoch and is immediately reliable.

In the figures corresponding to the following examples,

B. Wheel Slip

The encoder approach assumes no slip. Wheel slip is defined by the equation $s = v - Rw$, where v is the linear velocity of the wheel center, R is the wheel radius, and w is the rotational rate of the wheel. For no-slip, $s = 0$ and the bottom contact point of the wheel with the ground is stationary. When $s \neq 0$, the bottom contact point of the wheel is slipping relative to the ground. In this case, the change in encoder counts integrated through the kinematic equations may not yield accurate predictions of vehicle motion.

In this example, at t_{45} the right wheel momentarily slips one-half of a full rotation faster than the left wheel, with no change in the *actual* heading. The yaw attitude error as well as wheel radii errors are shown in Figure 3. The dead-reckoning (DR) algorithm integrates the measured wheel rotations through the kinematics yielding a rapid heading change, which then stays constant as the DR implementation does not have a feedback mechanism. The EKF uses its feedback algorithm, and outlier algorithm described in Section III-C, to attempt to drive its residuals toward zero. In the process, the EKF significantly changes the wheel radii. The EKF performance does not recover within the time period illustrated. The full nonlinear MAP employs the same outlier algorithm described in Section III-C, adjusts for the error contained in the information vector, ζ of eqn. (31), and repeats the optimization until convergence. Here the MAP required only 2 additional iterations than nominal to recover performance.

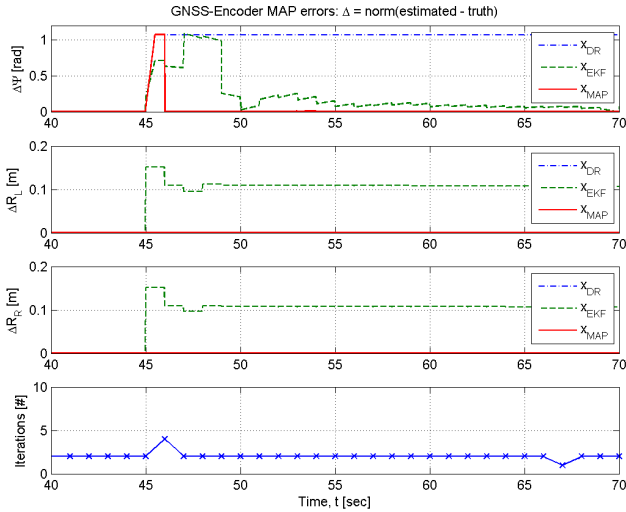


Fig. 3. Wheel slip induced error at $t=45$ sec. results in a constant 1 radian DR error. The EKF is unreliable for 40 sec., while the MAP immediately compensates.

C. Unequal Wheel Radii

The yaw attitude error and wheel radii errors are shown in Figure 4. At t_{45} the right wheel changes instantaneously to have a 10% smaller radius, simulating instantaneous unequal inflation pressure. The DR algorithm yields a continuous

heading change due to a difference in the encoder counts. The EKF adjusts the estimate of the wheel radii to account for the apparent reduction in encoder measurements. Its yaw attitude error persists for the duration of the simulation. The nonlinear MAP estimator is able to drive the yaw error back to (near) zero within 20 seconds, even though it does not drive the wheel radii errors back to zero. Once the radii errors are back within the unobservable space, they have no effect on the estimator performance and cannot be further improved. Just after $t = 75s$, as the vehicle turns, the unobservable space changes. The effect of this change is that the yaw and position errors grow and the MAP wheel radii estimation errors converge towards zero. Note that the number of iterations also increase in this time period. As the radii estimation errors converge to the new unobservable space, the yaw error converges toward zero, until the unobservable space changes again in the future.

Note that this result demonstrates that vehicle-level calibration of R_l and R_r [14], is no longer necessary under the MAP architecture. Instead, calibration is handled on-line while the vehicle undergoes continuous change throughout its lifetime.

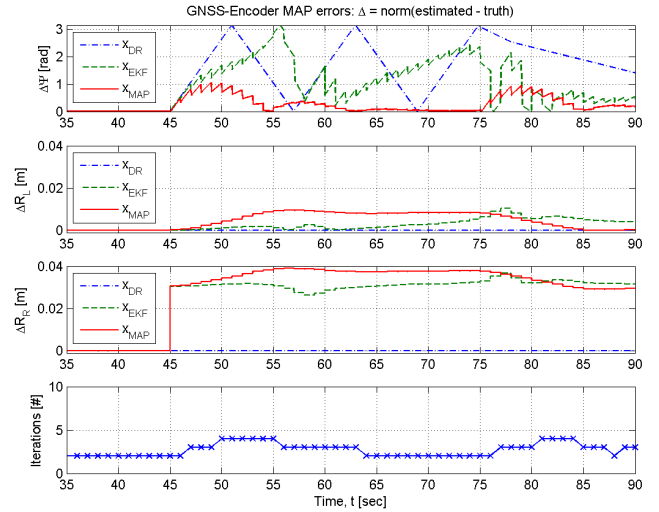


Fig. 4. A 10% right wheel radius reduction at $t=45$ s. causes a steadily increasing DR error. The EKF is unreliable for the duration of the simulation. The MAP compensates the estimated wheel radii, driving them to the unobservable space, yielding an accurate yaw within about 20 s.

D. Estimation of Grade

Estimation of grade is achieved through the estimation of both θ and vertical position d . This is shown as n and d position error and θ error in Figure 5. The DR algorithm has no means to detect grade, so $\theta = 0$, which leads to error not only in d and θ but longitudinal errors (n , e) as well. Both the EKF and MAP correctly estimate the value for θ and d .

E. GNSS Observation Error

Consider the case for the urban canyon or viaducts wherein the GNSS signals are subject to multi-path due to reflection, or distortion due to overhead foliage. Figure 6 demonstrates

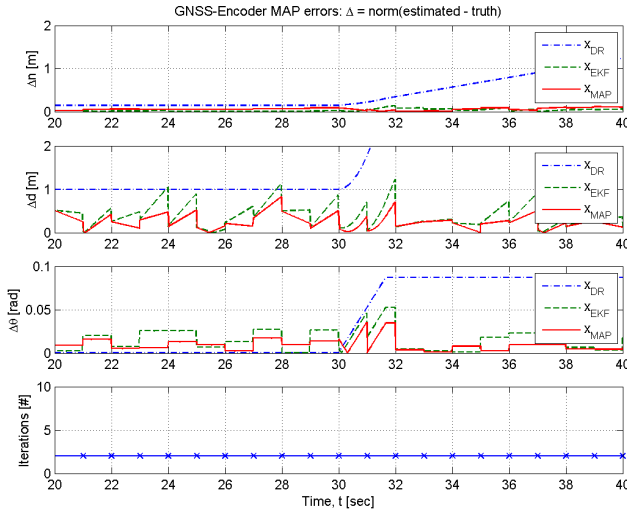


Fig. 5. The EKF and MAP correctly estimate θ and d as the vehicle transitions from level to climb starting at $t=30$ sec. The DR develops a steadily increasing 3D position error.

this case such that 3 of 8 GNSS satellite signals are corrupted between t_{45}, \dots, t_{46} producing a 2m position error for the EKF. Here the EKF position solution is inaccurate for 5 seconds, even after the GNSS signal has returned to normal. This is due to the EKF linearizing the model upon the prior state estimate.

The MAP identifies and removes outlier as described in Section III-C, maintaining a reliable position and attitude estimate throughout the period of corrupted data. It is important to notice the MAP optimization at the error onset requires only 2 additional iterations for a converged solution.

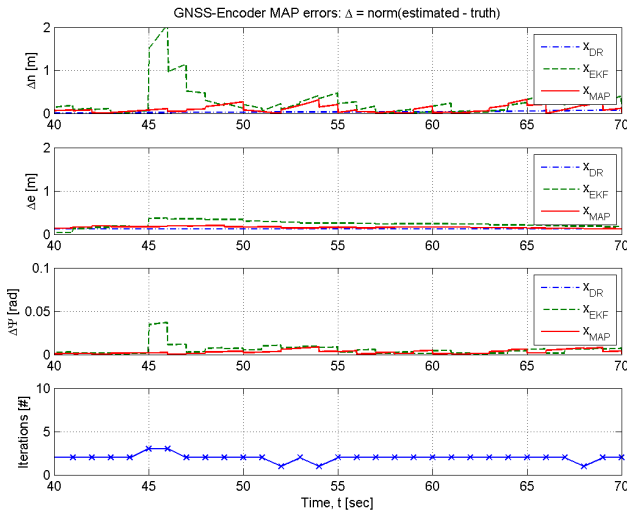


Fig. 6. A 2 meter GNSS outlier at $t=45$ sec., results in an EKF position error greater than 1 meter, and a solution which is unreliable for several seconds. Alternatively, the MAP outlier detection and removal algorithm required only one additional MAP iteration and is reliable throughout the event.

VI. CONCLUSIONS AND FUTURE WORK

In this paper we have presented a state estimation algorithm for GNSS-encoder navigation for wheeled vehicles. Using data over a sliding CRT window the real-time nonlinear MAP estimator provides a method by which anomalous measurement observations can be detected and removed with re-linearization, resulting in a more accurate state estimate. Our future work will provide real-world results.

VII. ACKNOWLEDGEMENTS

This research builds on the technical conversations with Dr. Yiming Chen. These technical collaborations are greatly appreciated.

REFERENCES

- [1] E. Abbott, J. D. Powell, *Land Vehicle Navigation Using GPS*, In Proceedings of the IEEE, volume 87, No. 1, pages 145–162, January 1999.
- [2] H. S. Bae, J. Ryu, and J. C. Gerdes, *Road Grade and Vehicle Parameter Estimation for Longitudinal Control Using GPS*, In IEEE Conference on Intelligent Transportation Systems, Proceedings, ITSC, pages 166–171, 2001.
- [3] J. Stephen and G. Lachapelle, *Development and Testing of a GPS-Augmented Multi-Sensor Vehicle Navigation System*, The Journal of Navigation, Royal Institute of Navigation, 54, no. 2, pages 297–319, 2001.
- [4] R. M. Rogers, *Improved Heading Using Dual Speed Sensors for Angular Rate and Odometry in Land Navigation*, In Proceedings of the Institute of Navigation National Technical Meeting, pages 353–361, 1999.
- [5] S. Zhao, Y. Chen, H. Zhang, and J. A. Farrell, *Differential GPS Aided Inertial Navigation: a Contemplative Realtime Approach*, in 19th IFAC World Congress, pages 8959–8964, 2013.
- [6] S. Zhao, Y. Chen, and J. A. Farrell, *High Precision 6DOF Vehicle Navigation in Urban Environments using a Low-cost Single-frequency GPS Receiver*, In Proceedings of IROS Workshop on Planning, Perception and Navigation for Intelligent Vehicles, 2014.
- [7] E. J. Rossetter and J. C. Gerdes, *The Role of Handling Characteristics in Driver Assistance Systems with Environmental Interaction*, In Proceedings of the 2000 ACC, Chicago, IL, pages 2528–2532, 2000.
- [8] A. T. van Zanten, *Evolution of Electronic Control Systems for Improving the Vehicle Dynamic Behavior*, In Proceedings of the 6th International Symposium on Advanced Vehicle Control, pages 1–9, 2002.
- [9] A. T. van Zanten, et al., *Vehicle Stabilization by the Vehicle Dynamics Control System ESP*, In Proceedings of the 1st IFAC conference on Mechatronic Systems, Darmstadt, Germany, pages 95–102, 2000.
- [10] D. C. Conner, P. R. Kedrowski, C. F. Reinholtz, *Multiple camera, laser range finder, and encoder data fusion for navigation of a differentially steered 3-wheeled autonomous vehicle*, In Proceedings SPIE, vol. 4195, Mobile Robots XV and Telemanipulator and Telepresence Technologies VII, pages 76–83, March 2001.
- [11] T. N. Hossein, S. Mita, L. Han, Q. H. Do, *Multi-Sensor Data Fusion for Autonomous Vehicle Navigation and Localization through Precise Map*, International Journal of Automotive Engineering, vol. 3, pages 19–25, 2012.
- [12] x. Li, W. Zhang, *An Adaptive Fault-Tolerant Multi-sensor Navigation Strategy for Automated Vehicles*, IEEE Transactions on Vehicular Technology, vol. 59, no. 6, pages 2815–2829, July 2010.
- [13] R. M. Rogers, *Land Vehicle Navigation Filtering for GPS/Dead-Reckoning System*, In Proceedings of the Institute of Navigation National Technical Meeting, pages 703–708, Jan. 1997.
- [14] J. Borenstein, L. Feng, *Measurement and Correction of Systematic Odometry Errors in Mobile Robots*, IEEE Transactions on Robotics and Automation, Vol. 12, No. 5, pages 869–880, October 1996.
- [15] J. A. Farrell, *Aided Navigation: GPS with High Rate Sensors*, McGraw Hill, 2008.
- [16] S. Zhao, Y. Chen, H. Zhang, J. A. Farrell, *Differential GPS Aided Inertial Navigation: a Contemplative Realtime Approach*, IFAC, pages 8959–8964, 2014.
- [17] H. Chiu, S. Williams, F. Dellaert, S. Samarasekera, R. Kumar, *Robust Vision-Aided Navigation Using Sliding-Window Factor Graphs*, ICRA, pages 46–53, 2013.
- [18] F. Dellaert, M. Kaess, *Square Root SAM: Simultaneous Localization and Mapping via Square Root Information Smoothing*, Int. J. Rob. Res., vol.25, no.12, pages 1181–1203, 2006.
- [19] M. Kaess, A. Ranganathan, F. Dellaert, *iSAM: Incremental Smoothing and Mapping*, IEEE Trans. Robotics, vol.24, no.6, pages 1365–1378, 2008.
- [20] S. M. Kay, *Fundamentals of Statistical Signal Processing: Estimation Theory*, Prentice Hall Signal Processing Series, New York 2013.